ADVANCED MATERIALS INTERFACES
Open Access
www.advmatinterfaces.de



# An Atomic-Scale View at $\gamma$'-$Fe_4N$ as Hydrogen Barrier Material

*Aleksander Albrecht, Sang Yoon Song, Su-Hyun Yoo, Chang-Gi Lee, Mathias Krämer, Marcus Hans, Baptiste Gault, Yan Ma, Dierk Raabe, Seok Su Sohn,* Yonghyuk Lee,* and Se-Ho Kim**

**Hydrogen, while a promising sustainable energy carrier, presents challenges such as the embrittlement of materials due to its ability to penetrate and weaken their crystal structures. Here $\gamma$'-$Fe_4N$ nitride layers, formed on iron through a cost-effective gas nitriding, are investigated as an effective hydrogen permeation barrier. The relatively short process carried out at 570 °C consisted of pre-nitriding in an atmosphere with higher nitriding potential, followed by treatment in a nitriding potential of 0.0016 $Pa^{-1/2}$ to obtain a pure $\gamma$' layer. A combination of screening methods, including atom probe tomography, density functional theory calculations, and hydrogen permeation analysis, revealed that the nitride layer reduces hydrogen diffusion (steady-state hydrogen flux 3.21 x $10^{-8}$ mol/$m^2$·s) by a factor of 20 compared to pure iron, at room temperature. This reduction is achieved by creating energetically unfavorable states due to stronger hydrogen-binding at the surface and high energy barriers for diffusion. The findings demonstrate the potential of $\gamma$'-$Fe_4N$ as a cost-efficient and easy-to-process solution to protect metallic materials exposed to hydrogen at low temperatures, with great advantages for large-scale applications.**

## 1. Introduction

Hydrogen can be a blessing or a curse. It has high potential to become a versatile, sustainable energy carrier and play a key role in global decarbonization efforts. However, being one of the smallest elements, hydrogen is difficult to detect and control, and it can penetrate the microstructure of solid materials, leading to unpredictable and catastrophic loss in ductility and tensile strength, an effect known as H embrittlement (HE).[1–3] Despite multiple efforts to design HE-resistant alloys, key infrastructure components such as pipelines, valves, and welded joints remain vulnerable to HE and permeation due to the high diffusivity of hydrogen in body-centered cubic (bcc) iron alloys.[4–6] For instance, owing to the high diffusivity of bcc steels, as much as 0.4% of

A. Albrecht
Department of Inorganic Chemical Technology and Environment Engineering
Faculty of Chemical Technology and Engineering
West Pomeranian University of Technology in Szczecin
Piastów Ave. 42, Szczecin 71-065, Poland

A. Albrecht, M. Krämer, B. Gault, Y. Ma, D. Raabe, S.-H. Kim
Max Planck Institute for Sustainable Materials
Max-Planck-Straße 1, 40237 Düsseldorf, Germany
E-mail: sehonetkr@korea.ac.kr

S. Y. Song, C.-G. Lee, S. S. Sohn, S.-H. Kim
Department of Materials Science and Engineering
Korea University
Seoul 02841, Republic of Korea
E-mail: sssohn@korea.ac.kr

The ORCID identification number(s) for the author(s) of this article can be found under https://doi.org/10.1002/admi.202500207



**DOI: 10.1002/admi.202500207**

S.-H. Yoo
Korea Research Institute of Chemical Technology
Daejeon 34114, Republic of Korea

M. Hans
Materials Chemistry
RWTH Aachen University
Kopernikusstr. 10, 52074 Aachen, Germany

B. Gault
Chemical Data-Driven Research Center
Korea Research Institute of Chemical Technology
Daejeon 06211, Republic of Korea

Y. Ma
Department of Materials Science and Engineering
Delft University of Technology
Mekelweg 2, Delft 2628 CD, The Netherlands

Y. Lee
Department of Chemistry and Biochemistry
University of California Los Angeles
Los Angeles, CA 90095, USA
E-mail: yonghyuklee@g.ucla.edu

H can get lost through a pipeline during operation.[7] An effective solution to mitigate these issues is the application of barrier coatings or gettering layers to suppress hydrogen permeation.[8–19]

Nitriding of iron-based materials is a well-known process.[20] It involves implementing nitrogen into the interstitial sites of the iron lattice in the near-surface region. A layer of nitrides (e.g. $\gamma'$-$Fe_4N$ and/or $\varepsilon$-$Fe_{3-2}N$), called a compound layer, can be created during diffusion-controlled growth, depending on the element's partial pressure. Beneath it, a volume of N-saturated iron with a possible minor contribution of nitride precipitates is created, which is called a diffusion zone. Depending on the base material (mostly its structure and concentration of alloying elements) and process conditions (in conventional processes mainly the nitriding potential $r_N = p_{NH_3} / p_{H_2}^{3/2}$, temperature, time), different microstructures of the compound layer and diffusion zone may be obtained.

For HE application, face-centered cubic (fcc, austenitic) steels exhibit lower hydrogen diffusivity due to their densely packed structure but higher solubility.[21] This characteristic can be exploited to make fcc steels more resistant to HE.[22,23] In contrast, ferritic and martensitic bcc steels have low hydrogen solubility but higher hydrogen diffusivity, enabling rapid diffusion during deformation, thereby increasing susceptibility to hydrogen-assisted cracking.[24]

Austenitic steels also have higher nitrogen solubility, which enables the formation of the stable $\gamma'$-$Fe_4N$ nitride phase[25] during nitriding, offering improved resistance to HE compared to the more brittle $\varepsilon$-$Fe_{3-2}N$ phase that can form in bcc steels.[26] While bcc steels are generally less expensive to produce, the introduction of a stable $\gamma'$-$Fe_4N$ structure on a surface through nitriding could significantly improve their corrosion resistance and mechanical properties against HE, broadening their applicability in a more demanding environment.

Various applications of nitriding have been reported to have a positive influence on wear resistance, tribological properties, and corrosion resistance,[20] along with barrier properties against hydrogen uptake of iron-based materials.[27,28] It was shown that surface layers of nitrides have a profound impact on the permeability of hydrogen through the nitrided iron-based material. Other studies focused more on the mechanisms of hydrogen absorption and transport in pure iron.[29–31] highlighting the separate influence of the reduction of hydrogen ingress (surface effect) and its transport (barrier effect).

The positive effect of nitriding on HE resistance was confirmed in high-strength low-alloyed bcc pipeline steel.[32,33] low-alloyed bcc AISI 4140 steel.[28] bcc structural nitriding steel,[34] ultra-high-strength bcc AISI 4340 steel,[35] low-alloyed bcc ASTM A387 Grade 22 steel,[36] fcc AISI 304 stainless steel,[19] and duplex stainless steel.[37] While studies have reported on the influence of nitride and non-nitrided layer thickness on hydrogen permeation, the absence of detailed microstructural characterization has limited the ability to fully assess the nitride state.[30,38] In previous works, the influence of nitrided layer structure, i.e. porous or dense compound layers of hexagonal $\varepsilon$-$Fe_{3-2}N$ + fcc $\gamma'$-$Fe_4N$ nitride, layers of pure fcc $\gamma'$ nitride, as well as separated diffusion layers of iron with dispersed nitride phase, was examined.[39,40] The lowest hydrogen uptake and permeation were shown for $\varepsilon+\gamma'$ compound layers, yet at the same time, this type of layer is most susceptible to porosity caused by nitrogen desorption, which can induce layer fracturing and a drastic decrease in barrier properties. Promising experimental results led to theoretical calculation of the interaction of hydrogen with $\alpha$-Fe, $\gamma'$-$Fe_4N$, $\varepsilon$-$Fe_3N$, and $\varepsilon$-$Fe_2N$ structures using first-principles calculations through density functional theory (DFT).[35,41] Further improvements were also suggested by combining nitriding with e.g., carbon, oxygen, sulfur, and boron.[42,43]

Although the hydrogen permeation of iron alloys and several hydrogen barrier coating technologies have been investigated, their implementation remains limited due to a lack of comprehensive mechanistic understanding and challenges in scaling the current technique.[39,44,45] This seems a bit counterintuitive, since nitriding of bulk iron-based materials is a well-established technology, with many companies producing both nitriding equipment and nitrided parts, thus making it inexpensive to create nitride layers on large workpieces. The above-mentioned works used either ion implantation or plasma nitriding, and an attempt to use more facile gas nitriding also proved successful.[38]

Each of these methods has its advantages. Ion implantation, mainly used in the semiconductor industry, is based on penetrating the treated material in an evacuated chamber with a beam of accelerated nitrogen ions. This method allows for nitriding without additional heat sources, reduces use of gas substrates and emissions, omits hydrogen introduction into the material, might not require surface activation, which is especially important in the case of stainless steel, yet usually yields relatively thin nitride layers, in the range of up to several microns, and requires high investment costs.[19,20,27] In plasma nitriding, pulsed DC voltage is applied to a mixture of $N_2$ and $H_2$ in an evacuated chamber containing the treated material. Plasma treatments allow for good control of processes even on stainless steels, are more eco-friendly than conventional nitriding, as they are quicker and do not require ammonia and consume minimal amounts of substrate gases, yet they usually require surface activation, and, like ion implantation, they involve high investment costs.[40,46] Gas nitriding of heated material in the atmosphere of $NH_3$ and $H_2$ is the simplest and best studied of these methods, allowing for good process control and numerous optimization possibilities, while keeping the lowest investment costs.[47] The main drawbacks of this method, high energy and gas consumption, and relatively high emissions, may be significantly reduced by tailoring the parameters of the process.[48]

In this study, we adopted a simple and cost-effective gas nitriding approach using a controlled mixture of ammonia ($NH_3$) and hydrogen ($H_2$) to nitride pure $\alpha$-Fe. This method offers significant potential for industrial scalability while enabling the formation of a thin yet continuous $\gamma'$-$Fe_4N$ layer within a short processing time. To comprehensively evaluate the effectiveness of $\gamma'$-$Fe_4N$ as a hydrogen permeation barrier, we conducted atomic-scale investigations using atom probe tomography (APT), complemented by permeation tests and DFT calculations. Our results aim to provide a fundamental understanding rather than addressing a specific engineering scenario or industrial working condition. This integrated approach thus offers insights into the intrinsic properties and mechanisms underpinning the performance of $\gamma'$-$Fe_4N$ as a potential hydrogen barrier material.

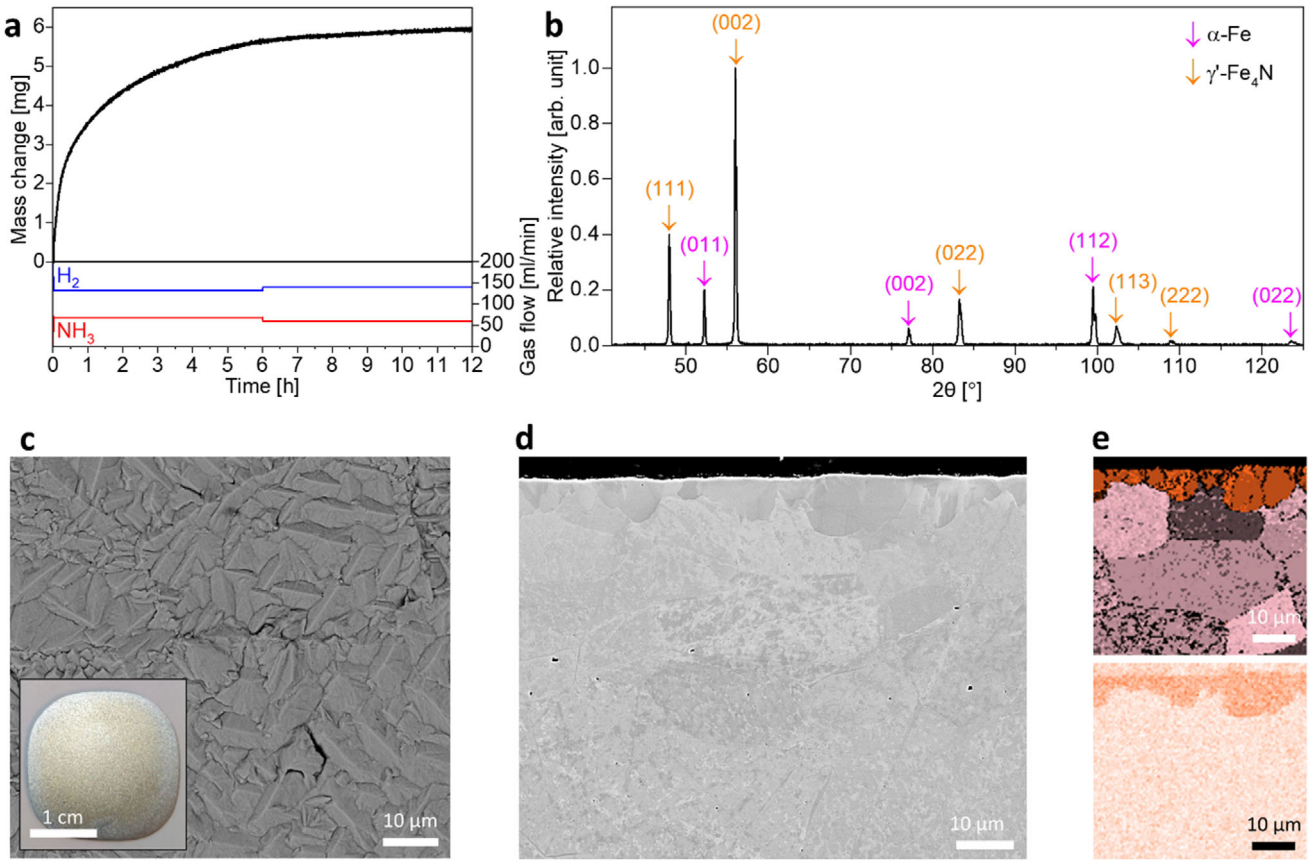


**Figure 1.** a) Characterization of as-designed $Fe_4N$@Fe sample. b) XRD measurement: pink (BCC $\alpha$-Fe) and orange (FCC $\gamma'$-$Fe_4N$). c) Surface morphology. The inset shows the photograph of the $\gamma'$-$Fe_4N$ layer on an $\alpha$-Fe membrane. d) Cross-sectional SEM image of the as-synthesized $Fe_4N$@Fe and corresponding e) EBSD measurement (FCC in orange and BCC in pink) and EDS of nitrogen (in orange) content map. Experimental details can be found in the Experimental Sections.

## 2. Results and Discussion

A pure polycrystalline $\alpha$-iron plate (100mm x 100 mm x 1 mm, MaTeck, purity >99.5%) was cut to a diameter of ca. 24 mm and polished with a 3 µm diamond suspension finish. Prior to the nitriding process, the foil was recrystallized at 650 °C in an $H_2$ environment (99.999% purity, Messer Poland) for 2 h to remove stresses coming from rolling, then polished mechanically to 1 µm diamond suspension finish and chemically with Nital 1% (1 vol% $HNO_3$ in ethanol). Subsequently, in a separate reactor of a thermobalance, the passive oxide layer created during transport was removed at 570 °C in the $H_2$ atmosphere. Then the mixture of $NH_3$ (99.998% pure, Air Liquide Poland) and $H_2$ gases was introduced into the chamber for the nitriding process at 570 °C (Floe-like method, based on works of Somers et al.).[49,50] The total gas flow, controlled with a set of mass flow regulators, was sustained at 200 ml/min. The process was carried out under ambient pressure. Initially, the material was subjected to a pre-nitriding atmosphere consisting of 34 vol.% of $NH_3$ for 6 h. The higher nitriding potential (0.0020 $Pa^{-1/2}$) is used to reduce the incubation time for $\gamma'$-$Fe_4N$ phase formation.[51] Then, the $NH_3$ concentration was lowered to the desired value of 30 vol% (0.0016 $Pa^{-1/2}$) for another 6 h to obtain a layer of pure $\gamma'$-$Fe_4N$. This procedure was selected from a number of preliminary test conditions with the same base material. The final $NH_3$ concentration was set near the middle of the $\gamma'$-$Fe_4N$ region of the phase diagram at 570 °C[52,53] as a balance between nitriding rate (the higher potential, the quicker nitriding) and reducing the risk of porosity formation in oversaturated material due to recombination of $N_2$ in the volume of the material. It is also important to consider compensating for the reduction of local nitriding potential due to nitrogen recombination and desorption of $N_2$ from the surface of the nitrided material. The nitriding time was intentionally restricted to further avoid porosity caused by $N_2$ development. A shorter process is also beneficial for economic reasons. **Figure 1a** presents the measured mass changes of the material during the process. After the treatment, the sample was cooled in a nitriding atmosphere to prevent nitride decomposition. After reaching room temperature, the atmosphere was changed into a mixture of 0.0025 vol% of oxygen in nitrogen. The as-prepared sample was named $Fe_4N$@Fe.

The reflections corresponding to 48.0°, 56.0°, 83.3°, and 102.7° of $2\theta$ in the X-ray diffractogram (XRD) qualitatively confirm the presence of the $\gamma'$-$Fe_4N$ phase, as shown in Figure 1b. The relative intensity of the $\alpha$-Fe phase reflections, compared with intensities for well-crystallized and annealed iron (ICDD PDF4+ 04-007-9753), indicates a minor preferred orientation in the substrate material coming from incomplete recrystallization, which

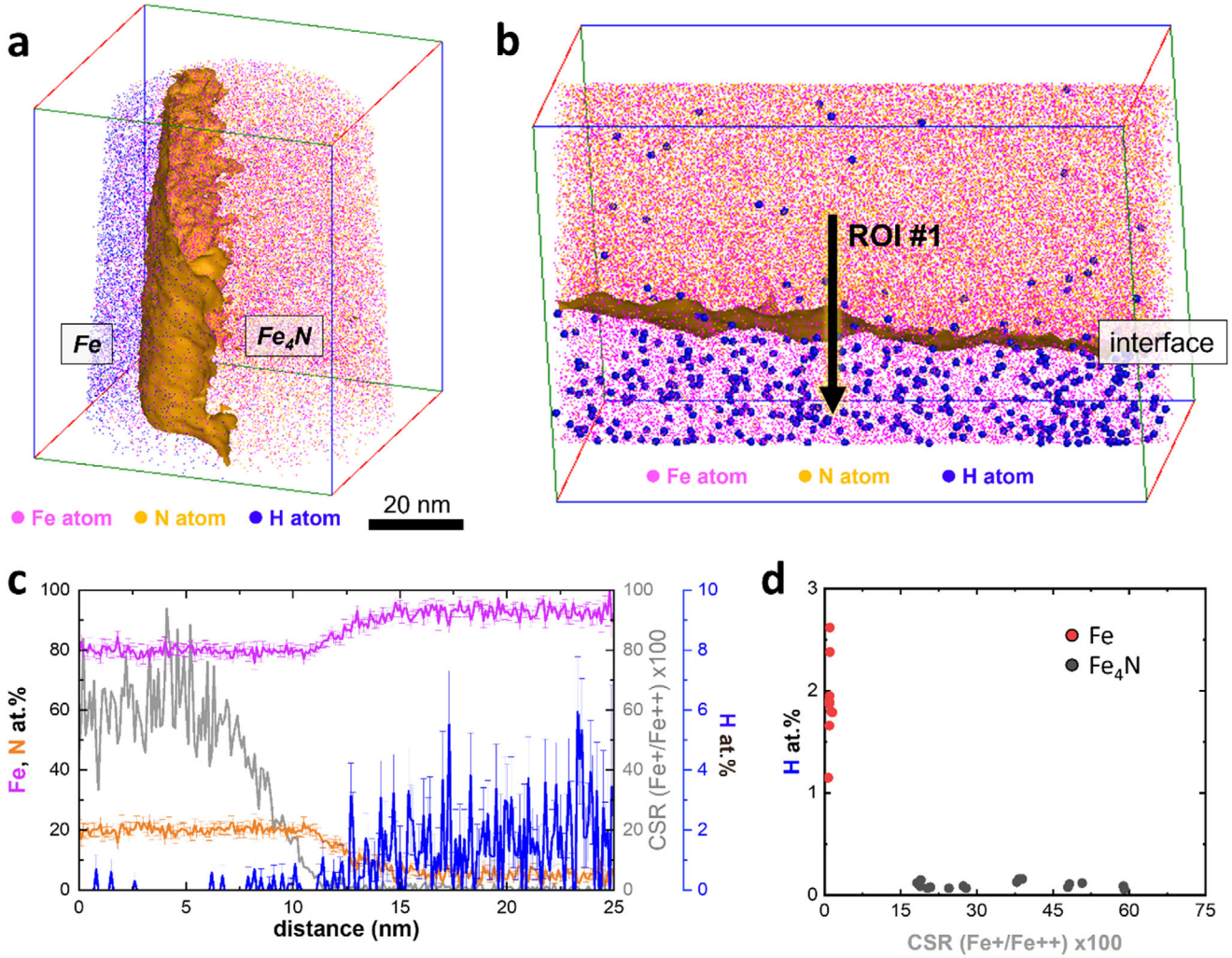


**Figure 2.** Atomic-scale characterization of as-designed $Fe_4N$@Fe sample a) 3D atom map of the $Fe_4N$@Fe and b) the extracted 10 × 30 × 50 $nm^3$ region. c) 1D compositional profiles of the elements along the region of interest (ROI) (ϕ15 nm x 25 $nm^3$). d) CSR vs. H concentration in $\alpha$-Fe and $\gamma'$-$Fe_4N$ region.

is confirmed by the EBSD analysis (see Figure S2, Supporting Information). For the $\gamma'$-$Fe_4N$ phase (compared to PDF4+ 00-064-0134), the preferred orientation is more pronounced, implying that the growth is anisotropic. For the $\gamma'$-$Fe_4N$ phase, the preferred orientation is more pronounced, implying that the growth is anisotropic. No other reflections related to the martensitic transformation of $\alpha''$-$Fe_{16}N_2$ and $\alpha'$-$Fe_8N$ are detected.[54] Figure 1c shows a scanning electron microscopy (SEM) image of the $Fe_4N$@Fe sample, where plate-like grains grew across the complete surface of the $\alpha$-Fe foil. To confirm the complete sealing of the foil, a cross-section was imaged by SEM as shown in Figure 1d. The region corresponding to the nitrided layer appears with no submicron-sized pores or cracks at the interface. Energy-dispersive X-ray spectroscopy (EDS) and electron backscatter diffraction (EBSD), presented in Figure 1e, were performed on the cross-section. For the $\alpha$-Fe foil, the average grain size is 41.7 ± 8.6 µm. Both techniques agree that the average thickness of the $\gamma'$-$Fe_4N$ layer is ≈5 µm. EBSD reveals that $\gamma'$-$Fe_4N$ grains can be up to ca. 8.9 µm in diameter, the average size of grains is 3.4 ± 2.4 µm, and both phases are the only phases in the material, and no delamination between them is observed.

The targeted $Fe_4N$@Fe interface was analyzed by APT (**Figure 2a**). An iso-composition surface with a threshold of 15 at.% N highlights the interface between the base $\alpha$-iron and the $\gamma'$-$Fe_4N$ phase. The measured hydrogen (H) content in $\gamma'$-$Fe_4N$ was 2 to 3 orders of magnitude lower than that in the $\alpha$-Fe. The detected hydrogen likely originated either from residual hydrogen gas in the chamber, from hydrogen absorbed/adsorbed during sample transfer and preparation of APT specimens, or from pre-existing hydrogen atoms in the materials, as summarized recently.[55] The H-signal from residual gases varies strongly with the intensity of the electrostatic field at the specimen surface during the analysis. This field can be assessed based on a charge-state ratio (CSR), for instance,[56] and in general, higher electric fields result in lower H signals from the residual background.[55] Ten ROIs (10×10×10 $nm^3$ in volume) were extracted from

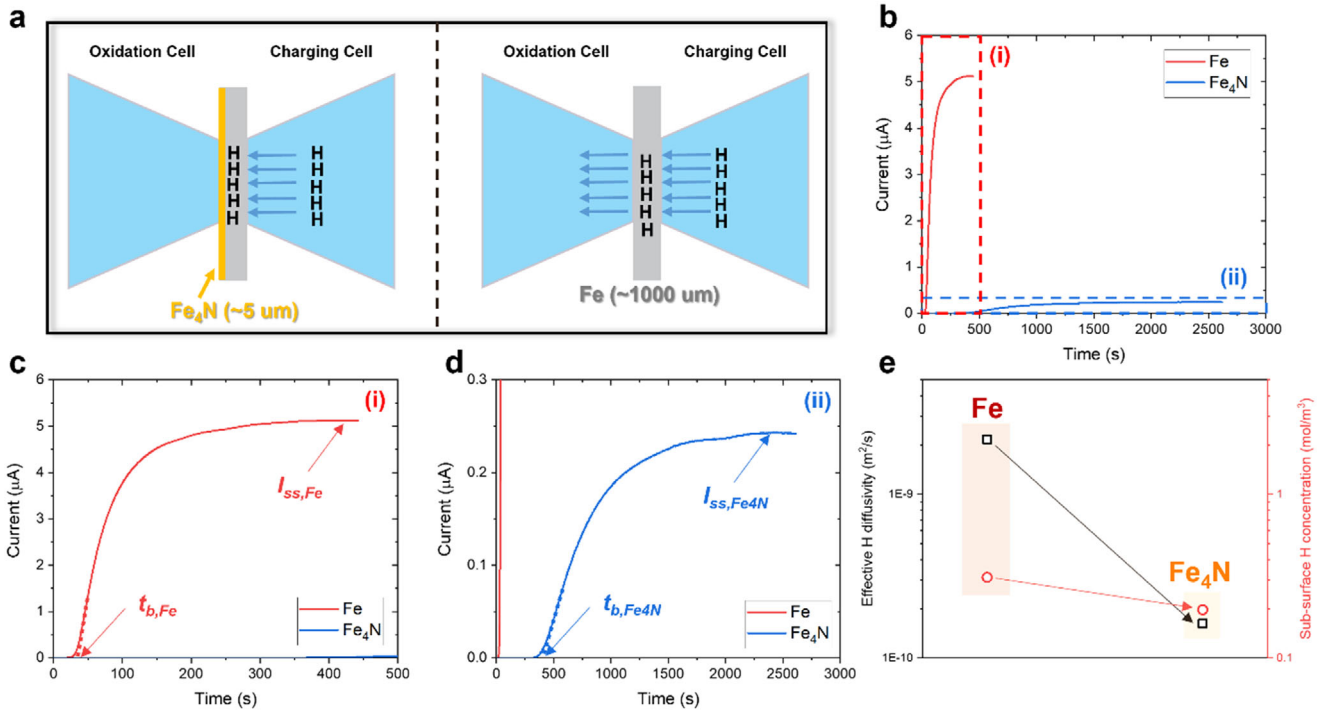


**Figure 3.** H-cell permeation experiment. a) Schematic illustration of hydrogen permeation experiments of the Fe and as-designed $\gamma'$-$Fe_4N$ membranes. b) Hydrogen permeation curves of the Fe (red) and $Fe_4N$@Fe (blue). c,d) Enlarged view of dashed red and blue lines in (b), respectively. e) Logarithmic plot of effective hydrogen diffusivity ($D_{eff}$) and sub-surface H concentration ($C_{0R}$) with the same scale range of Fe and $Fe_4N$ coated membranes.

$\alpha$-Fe and $\gamma'$-$Fe_4N$ phases to plot CSR vs. H content. The results supported the expected trend[57] where higher fields, i.e., higher $Fe^+/Fe^{++}$ CSR, are more likely to result in lower H content. However, an unusually low and constant H content (0.07 at.%) was measured in the $\gamma'$-$Fe_4N$ phase over a range of different CSR, as shown in Figure 2b,c (see Figure S1, Supporting Information for details, where a similar observation was found in another $\gamma'$-$Fe_4N$ APT dataset, showing very low H content as well). This suggests that the $\gamma'$-$Fe_4N$ phase itself possesses an intrinsic property of extremely low absorption/adsorption affinities, indicating that most hydrogen detected in APT measurements may originate from hydrogen contamination of materials rather than background hydrogen gas alone.[58]

A hydrogen permeation test was performed for the reference $\alpha$-Fe membrane and a nitrided membrane with a thickness of 1 mm using a hydrogen-cell apparatus. The cell consists of two electrochemical compartments, as schematically shown in **Figure 3**a. In the first compartment, hydrogen charging is performed in a solution of 3 wt% NaCl + 0.3 wt% $NH_4SCN$ with a high current density of 5 mA $cm^{-2}$ at room temperature. During electrochemical charging, the hydrogen produced at the cathode side diffuses through the sample to the other side, where the generated electrons from the electrochemical reaction are precisely detected as a current in the 'oxidation' compartment and recalculated to determine the amount of hydrogen diffusion. The corresponding hydrogen-permeation curves are plotted in Figure 3b–d. The reference $\alpha$-iron foil was tested, and within 20 s the current started to increase, indicating the amount of hydrogen penetrating through the sample with time. A saturation point was rapidly reached after 120 s. The effective hydrogen diffusivity ($D_{eff}$) and sub-surface hydrogen concentration ($C_{0R}$) of pure iron are calculated to be $2.16 \times 10^{-9}$ $m^2$ $s^{-1}$ and 0.31 mol $m^{-3}$, respectively, similar to the value reported in ref. [59,60] (see Experimental Sections for the details of the calculation).

For the $Fe_4N$-grown membrane, no increase in current was measured until 300 s of operation, indicating low H diffusion, with saturation after 2500 s. The calculated values of $D_{eff}$ and $C_{0R}$ are $1.62 \times 10^{-10}$ $m^2$ $s^{-1}$ and 0.19 mol $m^{-3}$, respectively, for the $Fe_4N$@Fe membrane. Moreover, the saturated H-flux ($J_{ss}$) is ≈20 times lower than that of pure Fe foil ($J_{ss\_Fe4N} = 3.21 \times 10^{-8}$ mol $m^{-2}$·s and $J_{ss\_Fe} = 6.75 \times 10^{-7}$ mol $m^{-2}$·s). Both membranes have a similar thickness and are subjected to the same charging condition, which indicates an identical hydrogen activity at the charged thin surface during the permeation test.[61] As the H permeability is a flux-based property affected by the membrane thickness and hydrogen activity, the same membrane thickness and charging condition indicate that the measured $J_{ss}$ is directly proportional to the H permeability of the membranes. Hence, it is reasonable to conclude that $\gamma'$-$Fe_4N$ has the ability to reduce H permeability by 20 times at room temperature with a thin film of ≈5 μm in thickness. Moreover, the significant decrease in $D_{eff}$ with $\gamma'$-$Fe_4N$ compared with $C_{0R}$, which is clearly shown in Figure 3e, indicates that such low H permeability of the $\gamma'$-$Fe_4N$ layer stems from diffusivity rather than solubility. The effective H diffusivity in the $\gamma'$-$Fe_4N$ layer was calculated to be $8.8 \times 10^{-13}$ $m^2$ $s^{-1}$ (diffusivities of previously reported hydrogen barrier materials are denoted in the Supporting Information), which is ≈4 orders lower than the pure iron ($2.16 \times 10^{-9}$ $m^2$ $s^{-1}$). This result confirms that the outstanding hydrogen blockage ability of $\gamma'$-$Fe_4N$ derives from inhibiting H diffusion.

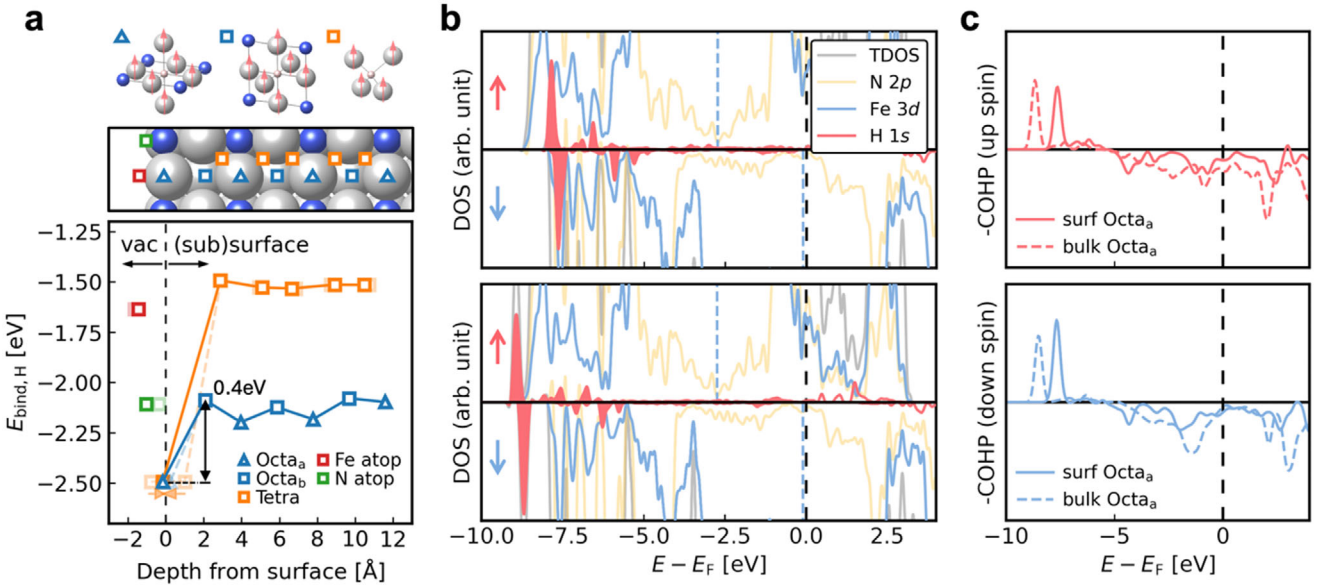


**Figure 4.** a) Calculated hydrogen binding energy ($E_{bind,H}$) as a function of the depth of H from the topmost N-rich $\gamma$'-$Fe_4N$(001) surface for various binding sites. The considered binding sites include octahedral site a ($Octa_a$), octahedral site b ($Octa_b$), tetrahedral site (Tetra) in the subsurface, and atop sites of surface Fe atom (Fe atop) and surface N atom (N atop). Configurations of the bulk adsorption sites and a side view of the atomic structure are illustrated in the upper panel. The initial positions of H before geometry relaxation are shown with pale markers. b) Up- and down-spin density-of-states (DOS) for H at the (top) surface and (bottom) bulk $Octa_a$ sites. Total DOS (TDOS), N 2*p*, Fe 3*d*, and H 1*s* states are represented by gray, yellow, blue, and red lines, respectively. Black dashed lines indicate the Fermi energy ($E_F$), and blue dashed lines mark the *d*-band center. c) Crystal orbital Hamilton population (COHP) analysis is presented for the (top) up-spin and (bottom) down-spin components.

To complement our experimental observations, we performed DFT calculations to investigate key aspects of H-diffusion resistance in $\gamma$'-$Fe_4N$ compared with $\alpha$-Fe. Although direct studies on $H_2$ dissociation on $Fe_4N$ remain unexplored, valuable insights can be drawn from investigations into nitrogen dissociation on nitrides and hydrogen dissociation on iron. Our analysis focused on the H-binding energies, $E_{bind,H}$, on $\gamma$'-$Fe_4N$ surfaces and their electronic structures, as illustrated in **Figure 4**. All computational methodologies used in the DFT calculations, along with the equations applied to compute thermodynamic quantities, are thoroughly detailed in the Experimental Sections. The high numerical convergence achieved with these computational settings is demonstrated in Figures S3 and S4 (Supporting Information). We employed (001) surfaces since they are favorable for growth on Fe(001) due to their structural resemblance and optimal magnetic and structural properties.[62–64] This choice is further supported by our XRD analysis (Figure 1b), which reveals a pronounced preferred orientation in the $\gamma$'-$Fe_4N$ phase, indicative of anisotropic growth favoring the (001) direction. Also, we mainly discuss the surface termination where both Fe and N atoms are exposed (N-rich) over the one containing only Fe atoms (termed Fe-rich) because of its superior thermodynamic stability (Figure S5, Supporting Information). Considering a range of H-binding sites (see Experimental Sections for details), we calculated the H-binding behavior from the topmost surface to the bulk-like subsurface. Lastly, we used a $p(2 \times 2)$ supercell to model $Fe_4N$(001) with a dilute hydrogen concentration, ensuring that the interaction between the hydrogen atoms in repeating images due to the periodic boundary condition is minimized (see Figure S3f, Supporting Information). As a result, the Zener sublattice ordering effects were found to have minimal influence on our calculations and thus were not explicitly considered in this context.[65]

As shown in Figure 4a, the surface $Octa_a$ site is the most stable over other surface and subsurface sites, and is even 0.34 eV lower than the H binding in the bulk (see Figure S3c, Supporting Information). The high stability of the surface $Octa_a$ site decays rapidly from the first subsurface site, which suggests a potential energy barrier for H penetration from the surface to beneath it. Intriguingly, substantial instability of tetrahedral sites is additionally observed. H binding in tetrahedral subsurface sites is roughly 0.63 eV less stable than those of octahedral subsurface sites, and hydrogen placed at the tetrahedral site ($H_{Tetra}$) near the surface transfers to the $Octa_a$ site during the structural optimization, indicating the infeasibility of subsurface $H_{Tetra}$. These findings suggest that H permeability inside $\gamma$'-$Fe_4N$ may be limited, as hydrogen must pass through the tetrahedral site to diffuse between neighboring octahedral sites with a minimum diffusion barrier of ≈0.63 eV.[45] Conversely, we note the high mobility of hydrogen within pure bcc Fe bulk, with a calculated diffusion barrier of ≈0.1 eV for H atoms moving between neighboring tetrahedral sites.[66–68] Although extrinsic factors such as grain boundaries and lattice distortions can further influence hydrogen transport, the atom probe data indicate that the number of mobile hydrogen atoms in $Fe_4N$ is inherently very low, underscoring that the dominant mechanism limiting diffusion is the intrinsic high activation energy and low hydrogen solubility in the nitride phase.

To further understand the origin of the high stability of the surface $H_{Octa_a}$, the calculated electronic structures are analyzed. The density-of-states (DOS) of the surface and the bulk $H_{Octa_a}$ are illustrated in Figure 4b (see Figure S6, Supporting

Information for the $H_{Octa_b}$ and $H_{Tetra}$ cases). Clear overlaps between Fe 3*d* and H 1*s* states for the surface $H_{Octa_a}$ indicate the formation of strong chemical bonds between interstitial H and neighboring Fe atoms, whereas isolations of H 1*s* have relatively weaker bonds for the bulk $H_{Octa_a}$. This isolation is more prominent for the down-spin components, which may contribute to the weaker binding since the down-spin *d*-band center is closer to the Fermi energy.[69–71] Furthermore, the crystal orbital Hamilton population (COHP) analysis in Figure 4c shows that more antibonding states of Fe–H bonds are observed for bulk $H_{Octa_a}$ near the Fermi level for both spins. These electronic structure analyses suggest that $\gamma$'-$Fe_4N$ exhibits H permeation resistance due to i) the stronger H binding on the surface hindering H penetration from the surface to the subsurface, and ii) the H diffusion barrier inside the bulk.

## 3. Conclusion

H has high potential as a sustainable energy carrier, but its tendency to cause embrittlement in materials like steel poses significant challenges. This study explores the use of a $\gamma$'-$Fe_4N$ nitride layer on $\alpha$-iron, produced through a cost-effective gas nitriding process, to create a hydrogen permeation barrier. The resulting $Fe_4N$@Fe material exhibited remarkable efficiency in blocking hydrogen at room temperature. An intriguing investigation of hydrogen distribution across $\gamma$'-$Fe_4N$ and $\alpha$-Fe interface was performed using APT, which indicates possible prevention of H adsorption and absorption. The DFT calculations provide a mechanistic understanding of the superior H-permeation resistance observed experimentally in $\gamma$'-$Fe_4N$, where it is energetically unfavorable for H to penetrate the surface, due to stronger H binding, and diffuse through the material, due to greater energy needed to pass between sites. The findings suggest that $\gamma$'-$Fe_4N$ can effectively block hydrogen penetration, making it valuable for large-scale applications.

## 4. Experimental Section

*Preliminary Result: Ammonia Reduction of Iron Ores*: Industrial hematite pellets were exposed to ammonia gas at 700 °C for 2 h and reduced to iron in a thermogravimetry analysis (TGA) setup. The progressive weight loss measured by TGA indicated the reduction of hematite into iron at 700 °C. During cooling to room temperature in ammonia gas, an increase in the weight of the sample was observed by TGA, suggesting the nitriding of reduced iron into nitrides. The X-ray diffraction and EBSD analyses confirmed that the sample consisted of 40 wt% $\gamma$'-$Fe_4N$ nitride.[72,73]

*Characterization of $Fe_4N$@Fe Material*: SEM imaging was performed with a Zeiss Sigma 500 microscope operating at 15 kV and 5.7 nA with a working distance of 10 mm. The EDS and EBSD measurements were taken simultaneously utilizing the EDAX/TSL system with Octane Elect and Hikari cameras at an accelerating voltage of 15 kV, a beam current of 5.7 nA, a scan step size of 0.5 µm, a specimen tilt angle of 70°, and a working distance of 15.5 mm. Data was processed with EDAX OIM Analysis v8.6 software.

Diffraction measurements were performed with Philips X'Pert Pro MPD apparatus with a Co tube working at 40 kV and 30 mA. The measurement was taken in a $2\theta$ range of 41–126°. Data were analyzed with PANalytical Highscore+ 3.0 software paired with the ICDD PDF4+ 2022 database. The raw data was shifted with a known displacement correction of 1 mm.

The sample for the APT measurement was prepared with a site-specific method using Gallium focused ion beam (FEI Helios Nanolab 600i).[74] 3D mapping was done with the use of CAMECA LEAP 5000 XR APT instrument in laser mode, at a temperature of 60K, 0.5% detection rate, 125 kHz pulse repetition rate, and laser energy of 40–60 pJ. The data reconstruction was performed with the AP Suite 6.1 software.

*H-Permeation Measurements*: H-permeation tests were performed to measure effective H diffusivity ($D_{eff}$), steady-state hydrogen flux ($J_{ss}$), and the sub-surface concentration ($C_{0R}$) of the reference $\alpha$-iron sample and $Fe_4N$@Fe sample. All three variables were calculated based on the ISO 17081.[75] The membrane sample (thickness: 1 mm, tested area: 78.5 $mm^2$) was placed between the H-oxidation cell and the H-charging cell. For reference $\alpha$-iron sample, both sides of the membrane were polished up to 4000 grit SiC paper. For the $Fe_4N$@Fe sample, one of the sides remained unpolished to preserve the $\gamma$'-$Fe_4N$ layer. To obtain effective H diffusivity, the following equation was used:

$$D_{\text{eff}} = \frac{L^2}{15.3 t_b} \tag{1}$$

where L is the sample thickness, and $t_b$ is the break-through time, which refers to the intersection point of the time axis and the line tangent to the inflection point of the permeation curve. The steady-state hydrogen flux ($J_{ss}$) was obtained by

$$J_{SS} = \frac{\frac{I_{SS}}{A}}{F} \tag{2}$$

where $I_{ss}$ is the steady-state current, A is the tested area, and F is the Faraday constant. The sub-surface concentration ($C_{0R}$) was expressed as

$$C_{0R} = \frac{J_{SS} \times L}{D_{\text{eff}}} \tag{3}$$

The diffusivity of the $\gamma$'-$Fe_4N$ layer was calculated by the equation for the layered materials, simply following the rule of mixture,[76]

$$\frac{L}{D_{\text{eff}}} = \frac{L_1}{D_1} + \frac{L_2}{D_2} \tag{4}$$

where L1, L2, D1, and D2 denote the substrate thickness, coating thickness, diffusivity of the substrate, and diffusivity of the coating, respectively.

*Computational Details: Density-Functional Theory Calculations*: All spin-polarized Density-Functional Theory (DFT) calculations were executed employing a plane-wave basis set and optimized norm-conserving Vanderbilt pseudopotentials (ONCVPSP)[77] sourced from the PseudoDojo[78] repository, as implemented within the Quantum ESPRESSO software package.[79] The electronic exchange and correlation were described using the generalized gradient approximation (GGA) due to Perdew, Burke, and Ernzerhof (PBE).[80] To achieve a more accurate electronic structure of the $\gamma$'-$Fe_4N$ system, on-site Coulomb interaction (DFT+*U*) has been applied to the Fe 3*d* electrons using an effective Hubbard parameter ($U_{eff}$) via Dudarev's approach.[81] Here, $U_{eff}$ = 0.4 eV,[82] which was reported as an adequate value to describe the electronic and magnetic properties of $\gamma$'-$Fe_4N$. An initial spin polarization of 0.15 applied to both Fe atoms at the corner site and the face-centered site resulted in magnetic moments of 3.03 and 2.28 $\mu_B$, respectively, as shown in Figure S3a,b (Supporting Information), in good agreement with the reference values.[82]

The kinetic cutoff energy for expanding the wave function was set to 80 Ry, while the charge density employs a cutoff energy of 320 Ry. Brillouin-zone integrations were conducted on a k-point grid with reciprocal distances of 0.04 $Å^{-1}$, resulting in a Γ-centered (7 × 7 × 7) k-point grid for bulk $\gamma$'-$Fe_4N$.

Optimization of lattice parameters for bulk $\gamma$'-$Fe_4N$ was achieved by minimizing the stress tensor and all internal degrees of freedom until the external pressure drops below 0.5 kbar. Electronic and ionic relaxations continue until residual changes in total energy and all force components fall below $1.4 \times 10^{-2}$ meV and 0.3 meV $Å^{-1}$, respectively.

Surface calculations were conducted using periodic boundary conditions and supercell geometries, ensuring a minimum vacuum separation of 10 Å to mitigate unphysical interactions between adjacent images. Asymmetric (001) slab models within the sub-space of (2 × 2) surface unit cells were constructed, comprising 11 atomic layers of the $\gamma$'-$Fe_4N$ (001) surface with the bottom three layers held fixed at their bulk positions. Geometry optimization in slab calculations employs the Broyden-Fletcher-Goldfarb-Shanno (BFGS) minimization algorithm.[83–85] A dipole correction was applied perpendicular to the surface to mitigate spurious electrostatic interactions.[86]

Separately, symmetric slab models comprising 11 atomic layers were employed with the central three layers being fixed while the top and bottom four layers being relaxed to accurately compute the surface free energy of Fe-rich and N-rich terminations. The high numerical convergence achieved with these computational settings has been demonstrated in Figure S3 (Supporting Information).

*Ab Initio Thermodynamics*: To evaluate the relative stability of $\gamma$'-$Fe_4N$ (001) surface structures with both Fe-rich and N-rich terminations, dan ab initio thermodynamic approach was utilized.[87–89] he surfaces in thermodynamic equilibrium was considered with a nitrogen-containing gas phase and calculate the surface free energy, $\gamma_{surf}^{(001),\nu_s}$, for a structure with the (001) surface and chemical composition $\nu_s$ as follow:

$$\gamma_{surf}^{(001),\nu_s} = \frac{1}{2A^{(001)}}\left[G_{surf}^{(001),\nu_s} - \sum_s \nu_s^{(001),\nu_s}\mu_s\right] \quad (5)$$

In this equation, $G_{surf}^{(001),\nu_s}$ represents the Gibbs free energy of the surface system, which is modeled as a symmetric slab within a supercell having a surface unit-cell area $A^{(001)}$. The term $\nu_s$ describes the number of atoms of each species $s$ (i.e., Fe and N), while $\mu_s$ denotes the chemical potential of species $s$ within the system.

Assuming the surface was in equilibrium with the underlying bulk $\gamma$'-$Fe_4N$, the chemical potentials of Fe and N were constrained by the bulk Gibbs free energy of $\gamma$'-$Fe_4N$ ($G_{Fe_4N,\,bulk} = 4\mu_{Fe} + \mu_N$). The nitrogen chemical potential is further set by its equilibrium with a nitrogen gas-phase reservoir, given by $\mu_N = \frac{1}{2}E_{N_2} + \Delta\mu_N$. Here, $E_{N_2}$ is the total energy of an isolated $N_2$ molecule, including zero-point energy (ZPE) contributions.[90]

In the difference to Equation (1), the Gibbs free energies of the condensed phases can be approximated by the DFT-computed total energies, allowing Equation (1) to be reformulated as:

$$\gamma_{surf}^{(001),\nu_s}(\Delta\mu_N) = \frac{1}{2A^{(001)}}\left[E_{surf}^{(001),\nu_s} - \nu_{Fe}^{(001),\nu_s}E_{Fe_4N,bulk}\right] - \frac{1}{2A^{(001)}}\left[\left(\nu_N^{(001),\nu_s} - \frac{1}{4}\nu_{Fe}^{(001),\nu_s}\right)\left(\frac{1}{2}E_{N_2} + \Delta\mu_N\right)\right] \quad (6)$$

The calculated surface free energy is valid within the range where the $\gamma$'-$Fe_4N$ system is thermodynamically stable. The stability is constrained by the nitrogen chemical potential, $\mu_N$, which ranges from the formation energy of $\gamma$'-$Fe_4N$ to the energy of the $N_2$ molecule ($G_{Fe_4N,\,bulk} - 4G_{Fe,BCC} - \frac{1}{2}E_{N_2} < \Delta\mu_N < 0$).

To determine the binding energy, $E_{bind,H}$, of hydrogen dopants on the $\gamma$'-$Fe_4N$ surface, the following formula:

$$E_{bind,H} = \frac{1}{\nu_H}\left(E_{surf}^{H-Fe_4N} - E_{surf}^{Fe_4N} - \nu_H\mu_H\right) \quad (7)$$

where $E_{surf}^{H-Fe_4N}$ and $E_{surf}^{Fe_4N}$ are the DFT-calculated total energies of the H-doped and undoped $\gamma$'-$Fe_4N$ surface structures, respectively. This study compares the favorable hydrogen binding energies as a function of the binding site and depth from the surface. In our models, a single hydrogen atom was incorporated within the periodic boundary ($\nu_H = 1$). Consequently, the differences in hydrogen binding energy among these models were independent of $\mu_H$. Therefore, the atomic energy of hydrogen was used as a reservoir ($\mu_H = E_H$ ), so that the focus was on comparing the stabilities among H at various binding sites rather than absolute values.

*Details in Surface Structures and Hydrogen Binding Sites*: The $\gamma$'-$Fe_4N$ (001) surface can exhibit two distinct terminations. One termination was composed solely of Fe atoms (termed as Fe-rich), while the other included both Fe and N atoms (N-rich). Our analysis of the surface phase diagram (see Figure S4, Supporting Information) demonstrates that the N-rich termination consistently exhibits a lower surface energy than that of the Fe-rich termination across the entire nitrogen chemical potential range where bulk $\gamma$'-$Fe_4N$ was stable.

Due to surface cleavage and the corresponding rearrangement of magnetic moments, $\gamma$'-$Fe_4N$ (001) has two symmetry-inequivalent $Fe_6$ interstitial-octahedral sites, $Octa_a$ and $Octa_b$, in the Fe-N layer and the Fe layer, respectively. Additionally, there is an interstitial-tetrahedral site (Tetra) surrounded by four Fe atoms.

*Electronic Structures*: The *d*-band center is calculated by

$$E_{d-center} = \frac{\int_{-\infty}^{\infty} E * DOS(E)}{\int_{-\infty}^{\infty} DOS(E)} \quad (8)$$

where $E$ is the eigenenergy and DOS($E$) is the density-of-states of Fe 3*d*-states. To gain a deeper insight into the chemical bonding nature, Crystal Orbital Hamilton Population (COHP) analysis with the LOBSTER code.[91,92] Due to LOBSTER's limitation to Projected Augmented Wave (PAW) potentials, it was not possible to directly use our norm-conserving pseudopotential results. Consequently, additional single-point calculations were performed for the structures of interest, which were initially relaxed using Quantum Espresso, by employing the Vienna Ab-initio Simulation Package (VASP)[93,94] while adhering to the same computational settings. This approach allowed us to accurately project and sum the COHP interactions between hydrogen and its neighboring iron and nitrogen atoms, thereby enabling a clear distinction between bonding, nonbonding, and antibonding interactions.

## Supporting Information

Supporting Information is available from the Wiley Online Library or from the author.

## Acknowledgements

A.A., S.Y.S., and S.-H.Y. contributed equally to this work. The authors thank K. Angenendt, U. Tezins, C. Broß, and A. Sturm for their support of the SEM, FIB, and APT facilities at MPIE. AA is thankful to the Polish National Agency for Academic Exchange for financing the scholarship at MPIE, Düsseldorf in the years 2022–2023 as a part of the NAWA Bekker Programme, project no. BPN/BEK/2021/1/00349. MK acknowledges financial support from the German Research Foundation (DFG) through DIP Project No. 450800666. This research was supported by the Nano & Material Technology Development Program through the National Research Foundation of Korea (NRF) funded by the Ministry of Science and ICT(RS-2024-00450561). This work was supported by the Korea Institute of Energy Technology Evaluation and Planning (KETEP) and the Ministry of Trade, Industry & Energy (MOTIE) of the Republic of Korea (No. RS-2024-00401917). S.-H. Yoo acknowledges support from the basic project from the Korea Research Institute of Chemical Technology in the Republic of Korea (KK2551-10).

## Conflict of Interest

The authors declare no conflict of interest.

## Data Availability Statement

The data that support the findings of this study are available on request from the corresponding author. The data are not publicly available due to privacy or ethical restrictions.

## Keywords

electrolytic hydrogen charging, $Fe_4N$, hydrogen diffusion barrier, hydrogen imaging, nitriding steel

Received: March 8, 2025
Revised: May 5, 2025
Published online:

[1] S. M. Myers, M. I. Baskes, H. K. Birnbaum, J. W. Corbett, G. G. DeLeo, S. K. Estreicher, E. E. Haller, P. Jena, N. M. Johnson, R. Kirchheim, S. J. Pearton, M. J. Stavola, *Rev. Mod. Phys.* **1992**, *64*, 559.
[2] R. Kirchheim, *Prog. Mater. Sci.* **1988**, *32*, 261.
[3] J. K. Nørskov, F. Besenbacher, J. Bøttiger, B. B. Nielsen, A. A. Pisarev, *Phys. Rev. Lett.* **1982**, *49*, 1420.
[4] B. Salerno, Offshore bolt failures provide chance to display safety culture Offshore Magazine, **2018**.
[5] Y.-S. Chen, P.-Y. Liu, R. Niu, A. Devaraj, H.-W. Yen, R. K. W. Marceau, J. M. Cairney, *Microsc. Microanal* **2023**, *29*, 1.
[6] H. Li, R. Niu, W. Li, H. Lu, J. Cairney, Y.-S. Chen, *J. Nat. Gas Sci. Eng.* **2022**, *105*, 104709.
[7] Z. Fan, H. Sheerazi, A. Bhardwaj, A.-S. Corbeau, A. Castañeda, A.-K. Merz, D. C. M. Woodall, S. Orozco-Sanchez, D. J. Friedmann, *Hydrogen Leakage: A Potential Risk For The Hydrogen Economy*, Columbia Center on Global Energy Policy, New York, USA **2022**.
[8] Y. Ishikawa, V. Nemanič, *Vacuum* **2003**, *69*, 501.
[9] H. K. D. H. Bhadeshia, *ISIJ Int.* **2016**, *56*, 24.
[10] V. Nemanič, *Nucl. Mater. Energy* **2019**, *19*, 451.
[11] J. A. Fedchak, J. K. Scherschligt, S. Avdiaj, D. S. Barker, S. P. Eckel, B. Bowers, S. O'Connell, P. Henderson, *J. Vac. Sci. Technol. B* **2021**, *39*, 024201.
[12] M. Sefa, J. A. Fedchak, J. Scherschligt, *J. Vac. Sci. Technol., A* **2017**, *35*, 041601.
[13] J. Bowker, G. R. Piercy, *Metall Trans A* **1984**, *15*, 2093.
[14] M. Moshref-javadi, H. Edris, A. Shafyei, H. Salimi-Jazi, *Int. J. Hydrogen Energy* **2017**, *42*, 6409.
[15] K. Saito, S. Inayoshi, Y. Ikeda, Y. Yang, S. Tsukahara, *J. Vacuum Sci. Technol. A* **1995**, *13*, 556.
[16] S. Samanta, C. Singh, A. Banerjee, K. Mondal, M. Dutta, S. B. Singh, *Surf. Coat. Technol.* **2020**, *403*, 126356.
[17] C. Benvenuti, P. Chiggiato, F. Cicoira, V. Ruzinov, *Vacuum* **1998**, *50*, 57.
[18] S. Fite, I. Zukerman, A. B. Shabat, S. Barzilai, *Surf. Interfaces* **2023**, *37*, 102629.
[19] B. Garke, C. Edelmann, R. Günzel, J. Brutscher, *Surf. Coat. Technol.* **1997**, *93*, 318.
[20] E. J. Mittemeijer, *Thermochemical surface engineering of steels*, Woodhead Publishing, Amsterdam **2015**.
[21] M. A. Tunes, P. J. Uggowitzer, P. Dumitraschkewitz, P. Willenshofer, S. Samberger, F. C. Da Silva, C. G. Schön, T. M. Kremmer, H. Antrekowitsch, M. B. Djukic, S. Pogatscher, *Adv. Eng. Mater.* **2024**, *26*, 2400776.
[22] M. B. Djukic, G. M. Bakic, V. S. Zeravcic, B. Rajicic, A. Sedmak, R. Mitrovic, Z. Miskovic, *Procedia Struct. Integr.* **2016**, *2*, 604.
[23] O. Bouledroua, Z. Hafsi, M. B. Djukic, S. Elaoud, *Int. J. Hydrogen Energy.* **2020**, *45*, 18010.
[24] B. Sun, W. Lu, B. Gault, R. Ding, S. K. Makineni, D. Wan, C.-H. Wu, H. Chen, D. Ponge, D. Raabe, *Nat. Mater.* **2021**, *20*, 1629.
[25] S. Hertzman, R. Naraghi, S. Wessman, R. Pettersson, U. Borggren, J. Y. Jonsson, N. H. Pettersson, M. K. Karami, A. Kohan-Zade, *Metall. Mater. Trans. A* **2021**, *52*, 3811.
[26] Y.-X. Wang, M.-F. Yan, Z.-B. Chen, C.-S. Zhang, Y. You, *Acta Metall. Sin. (Engl. Lett.)* **2018**, *31*, 371.
[27] A. M. Brass, J. Chene, J. C. Pivin, *J. Mater. Sci.* **1989**, *24*, 1693.
[28] P. Bruzzoni, S. P. Brühl, B. J. A. Gómez, L. Nosei, M. Ortiz, J. N. Feugeas, *Surf. Coat. Technol.* **1998**, *110*, 13.
[29] T. Zakroczymski, N. Lukomski, J. Flis, *J. Electrochem. Soc.* **1993**, *140*, 3578.
[30] Z. Wolarek, T. Zakroczymski, *Acta Mater.* **2004**, *52*, 2637.
[31] Z. Wolarek, T. Zakroczymski, *Acta Mater.* **2006**, *54*, 1525.
[32] F. D. Fassini, M. A. Zampronio, P. E. V. De Miranda, *Corros. Sci.* **1993**, *35*, 549.
[33] A. H. Bott, S. P. Brühl, B. Gómez, M. A. Zampronio, P. E. V. Miranda, J. N. Feugeas, *J. Phys. D: Appl. Phys.* **1998**, *31*, 3469.
[34] J. Cwiek, M. Baczyñska, *Arch. Mater. Sci. Eng.* **2010**, *43*, 30.
[35] J. J. M. Jebaraj, D. J. Morrison, J. B. McLaughlin, I. I. Suni, *J. Electrochem. Soc.* **2014**, *161*, C261.
[36] R. Chellappandian, G. Jena, L. Neelakantan, I. Adlakha, *JOM* **2024**, *76*, 327.
[37] B. Gołębiowski, T. Zakroczymski, W. Świątnicki, *SSP* **2011**, *183*, 71.
[38] M. A. Zampronio, F. D. Fassini, P. E. V. De Miranda, *Surf. Coat. Technol.* **1995**, *70*, 203.
[39] A. Gajek, Z. Wolarek, T. Zakroczymski, *Corros. Sci.* **2012**, *58*, 260.
[40] Y. Sugawara, T. Kudo, *ISIJ Int.* **2023**, *63*, 1405.
[41] T. Watanabe, Y. Kunisada, N. Sakaguchi, *ChemPhysChem* **2019**, *20*, 1369.
[42] E. Lunarska, J. Michalski, *Mater. Corros.* **2000**, *51*, 841.
[43] T. Zakroczymski, N. Lukomski, J. Flis, *Corros. Sci.* **1995**, *37*, 811.
[44] M. Tamura, *JMSE-B* **2016**, *6*, 297.
[45] M. Wu, J. Wang, B. Xing, H. Zhu, *Int. J. Hydrogen Energy* **2023**, *48*, 29418.
[46] K.-M. Winter, J. Kalucki, D. Koshel, *Thermochemical Surface Engineering of Steels*, Elsevier, Amsterdam, Netherlands **2015**, 141.
[47] J. P. Lebrun, *Thermochemical Surface Engineering of Steels*, Elsevier, Amsterdam, Netherlands **2015**, 615.
[48] Y.-L. Zhou, F. Xia, A.-J. Xie, H.-P. Peng, J.-H. Wang, Z.-W. Li, *Coatings* **2023**, *13*, 1846.
[49] M. A. J. Somers, E. J. Mittemeijer, *Metall. Mater. Trans. A* **1995**, *26*, 57.
[50] M. A. J. Somers, *Metallurgical Transact. A* **1989**, *20*, 1533.
[51] E. J. Mittemeijer, M. A. J. Somers, *Thermochemical Surface Engineering of Steels*, Elsevier, Amsterdam, Netherlands **2015**, 113.
[52] E. Lehrer, *Z. Electrochem* **1930**, *36*, 383.
[53] H. Göhring, O. Fabrichnaya, A. Leineweber, E. J. Mittemeijer, *Metall. Mater. Trans. A* **2016**, *47*, 6173.
[54] B. Ma, G. Guo, J. Liu, F. Zhang, J.-P. Wang, *AIP Adv.* **2022**, *12*, 075218.
[55] B. Gault, A. Saksena, X. Sauvage, P. Bagot, L. S. Aota, L. T. Belkacemi, T. Boll, Y.-S. Chen, L. Daly, J. O. Douglas, M. J. Duarte, P. J. Felfer, R. G. Forbes, J. Fu, H. M. Gardner, R. Gemma, S. S. A. Gerstl, Y. Gong, S. Jakob, B. M. Jenkins, M. E. Jones, H. Khanchandani, P. Kontis, M. Krämer, M. Kühbach, R. K. W. Marceau, K. L. Moore, V. Nallathambi, B. C. Ott, T. Prosa, et al., *arXiv:2405.13158* **2024**, 13158.
[56] D. R. Kingham, *Surf. Sci.* **1982**, *116*, 273.
[57] R. P. Kolli, *Adv. Struct. Chem. Imag.* **2017**, *3*, 10.
[58] S.-H. Yoo, S.-H. Kim, E. Woods, B. Gault, M. Todorova, J. Neugebauer, *New J. Phys.* **2022**, *24*, 013008.
[59] B. Siberchicot, *J. Magn. Magn. Mater.* **2009**, *321*, 3422.
[60] A. Drexler, W. Siegl, W. Ecker, M. Tkadletz, G. Klösch, H. Schnideritsch, G. Mori, J. Svoboda, F. D. Fischer, *Corros. Sci.* **2020**, *176*, 109017.

[61] Q. Liu, A. D. Atrens, Z. Shi, K. Verbeken, A. Atrens, *Corros. Sci.* **2014**, *87*, 239.
[62] Š. Pick, P. Légaré, C. Demangeat, *Phys. Rev. B* **2007**, *75*, 195446.
[63] J. Li, Y. Jiang, T. Ma, C. Lu, Y. Xu, D. Yang, M. Yan, *Phys. B* **2012**, *407*, 4783.
[64] X. Li, *Iron Nitride Based Magnetoresistance Devices For Spintronic Applications Ph.D. dissertation, University of Minnesota, Minneapolis, MN, United States*, **2018**.
[65] S. Waseda, T. Hickel, J. Morthomas, P. Chantrenne, M. Perez, J. Neugebauer, Dissecting physics of carbon ordering in bcc iron, http://arxiv.org/abs/2407.20649 (accessed September, **2024**).
[66] D. E. Jiang, E. A. Carter, *Phys. Rev. B* **2004**, *70*, 064102.
[67] Y. A. Du, L. Ismer, J. Rogal, T. Hickel, J. Neugebauer, R. Drautz, *Phys. Rev. B* **2011**, *84*, 144121.
[68] Y. A. Du, J. Rogal, R. Drautz, *Phys. Rev. B* **2012**, *86*, 174110.
[69] M. T. Greiner, T. E. Jones, S. Beeg, L. Zwiener, M. Scherzer, F. Girgsdies, S. Piccinin, M. Armbrüster, A. Knop-Gericke, R. Schlögl, *Nature Chem.* **2018**, *10*, 1008.
[70] H. Zheng, H. Li, L. Luo, Z. Zhao, G. Henkelman, *J. Chem. Phys.* **2021**, *155*, 024703.
[71] A. Cao, J. K. Nørskov, *ACS Catal.* **2023**, *13*, 3456.
[72] Y. Ma, J. W. Bae, S. Kim, M. Jovičević-Klug, K. Li, D. Vogel, D. Ponge, M. Rohwerder, B. Gault, D. Raabe, *Adv. Sci.* **2023**, *10*, 2300111.
[73] M. Jovičević-Klug, Y. Ma, P. Jovičević-Klug, J. M. Prabhakar, M. Rohwerder, D. Raabe, *ACS Sustainable Chem. Eng.* **2024**, *12*, 9882.
[74] K. Thompson, D. Lawrence, D. J. Larson, J. D. Olson, T. F. Kelly, B. Gorman, *Ultramicroscopy* **2007**, *107*, 131.
[75] *Method of measurement of hydrogen permeation and determination of hydrogen uptake and transport in metals by an electrochemical technique*, 2nd Ed., B S I Standards, Switzerland Geneva, **2014**.
[76] P. E. V. De Miranda, F. D. Fassini, *J. Mater. Sci.* **1993**, *28*, 5148.
[77] D. R. Hamann, *Phys. Rev. B* **2013**, *88*, 085117.
[78] M. J. Van Setten, M. Giantomassi, E. Bousquet, M. J. Verstraete, D. R. Hamann, X. Gonze, G.-M. Rignanese, *Comput. Phys. Commun.* **2018**, *226*, 39.
[79] P. Giannozzi, S. Baroni, N. Bonini, M. Calandra, R. Car, C. Cavazzoni, D. Ceresoli, G. L. Chiarotti, M. Cococcioni, I. Dabo, A. Dal Corso, S. De Gironcoli, S. Fabris, G. Fratesi, R. Gebauer, U. Gerstmann, C. Gougoussis, A. Kokalj, M. Lazzeri, L. Martin-Samos, N. Marzari, F. Mauri, R. Mazzarello, S. Paolini, A. Pasquarello, L. Paulatto, C. Sbraccia, S. Scandolo, G. Sclauzero, A. P. Seitsonen, et al., *J. Phys.: Condens. Matter* **2009**, *21*, 395502.
[80] J. P. Perdew, K. Burke, M. Ernzerhof, *Phys. Rev. Lett.* **1996**, *77*, 3865.
[81] S. L. Dudarev, G. A. Botton, S. Y. Savrasov, C. J. Humphreys, A. P. Sutton, *Phys. Rev. B* **1998**, *57*, 1505.
[82] E. L. P. y Blancá, J. Desimoni, N. E. Christensen, H. Emmerich, S. Cottenier, *Phys. Status Solidi B* **2009**, *246*, 909.
[83] C. G. Broyden, *IMA J. Appl. Mathemat.* **1970**, *6*, 222.
[84] D. Goldfarb, *Mathemat. Comput.* **1970**, *24*, 23.
[85] D. F. Shanno, *Mathemat. Comput.* **1970**, *24*, 647.
[86] L. Bengtsson, *Phys. Rev. B* **1999**, *59*, 12301.
[87] K. Reuter, *Catal. Lett.* **2016**, *146*, 541.
[88] K. Reuter, M. Scheffler, *Phys. Rev. B* **2001**, *65*, 035406.
[89] T. Lee, A. Soon, *Nat. Catal.* **2024**, *7*, 4.
[90] K. K. Irikura, *J. Phys. Chem. Ref. Data* **2007**, *36*, 389.
[91] S. Maintz, V. L. Deringer, A. L. Tchougr eeff, R. Dronskowski, *J. Comput. Chem.* **2016**, *37*, 1030.
[92] R. Nelson, C. Ertural, J. George, V. L. Deringer, G. Hautier, R. Dronskowski, *J. Comput. Chem.* **2020**, *41*, 1931.
[93] G. Kresse, J. Furthmüller, *Phys. Rev. B* **1996**, *54*, 11169.
[94] G. Kresse, J. Hafner, *Phys. Rev. B* **1993**, *47*, 558.